

MEASUREMENTS OF STELLAR INCLINATIONS FOR KEPLER PLANET CANDIDATES II: CANDIDATE SPIN-ORBIT MISALIGNMENTS IN SINGLE AND MULTIPLE-TRANSITING SYSTEMS

TERUYUKI HIRANO¹, ROBERTO SANCHIS-OJEDA², YOICHI TAKEDA³, JOSHUA N. WINN², NORIO NARITA³, AND YASUHIRO H. TAKAHASHI^{3,4}

ABSTRACT

We present a test for spin-orbit alignment for the host stars of 25 candidate planetary systems detected by the *Kepler* spacecraft. The inclination angle of each star's rotation axis was estimated from its rotation period, rotational line broadening, and radius. The rotation periods were determined using the *Kepler* photometric time series. The rotational line broadening was determined from high-resolution optical spectra with Subaru/HDS. Those same spectra were used to determine the star's photospheric parameters (effective temperature, surface gravity, metallicity) which were then interpreted with stellar-evolutionary models to determine stellar radii. We combine the new sample with the 7 stars from our previous work on this subject, finding that the stars show a statistical tendency to have inclinations near 90°, in alignment with the planetary orbits. Possible spin-orbit misalignments are seen in several systems, including three multiple-planet systems (KOI-304, 988, 2261). Ideally these systems should be scrutinized with complementary techniques—such as the Rossiter-McLaughlin effect, starspot-crossing anomalies or asteroseismology—but the measurements will be difficult owing to the relatively faint apparent magnitudes and small transit signals in these systems.

Subject headings: planets and satellites: general – planets and satellites: formation – stars: rotation – techniques: spectroscopic

1. INTRODUCTION

The angle of the stellar spin axis with respect to the planetary orbital axis (spin-orbit angle) is an observable quantity that may be important for understanding the evolutionary history of exoplanetary systems. In order to explain the existence of close-in giant planets (hot Jupiters or Neptunes), various migration scenarios have been proposed, which differ in their predictions for the spin-orbit angle. Some theories, such as disk migration, predict that the stellar spin and planetary orbital axes should be well aligned (e.g., Lin et al. 1996). Other theories, such as planet-planet scattering or Kozai migration, predict a very wide range of spin-orbit angles (see, e.g., Wu & Murray 2003; Nagasawa & Ida 2011; Fabrycky & Tremaine 2007).

Most of the current measurements of the spin-orbit angle have been based on observations of the Rossiter-McLaughlin (RM) effect (e.g., Queloz et al. 2000; Ohta et al. 2005; Winn et al. 2005; Narita et al. 2007; Wolf et al. 2007; Hirano et al. 2011b) or photometric anomalies due to transits over starspots (e.g., Sanchis-Ojeda et al. 2011; Nutzman et al. 2011; Désert et al. 2011). These measurements have revealed a diversity of spin-orbit angles (e.g., Hébrard et al. 2008; Winn et al. 2009; Narita et al. 2009). This diversity has inspired many theoretical studies of the possible reasons for highly inclined planetary orbits (e.g., Lai et al.

2011; Naoz et al. 2011). The measurements have also revealed some possible patterns relating the spin-orbit angle and the properties of the host stars (Winn et al. 2010; Albrecht et al. 2012). However, the existing measurements have been almost exclusively restricted to close-in giant planets. This is simply because the preceding measurement techniques are best suited to relatively large planets, which produce stronger spectroscopic or photometric signals during a planetary transit. Thus, the spin-orbit relations for smaller planets have been unknown until recently.

An important step was taken by Schlaufman (2010), who demonstrated that the stellar inclination angle (the angle between the stellar spin axis and the line of sight) can be readily estimated for a large number of transiting exoplanetary systems, and used to probe spin-orbit alignment. The basic idea is to use estimates of the rotation velocity V and the projected rotation velocity $V \sin I_s$ to determine $\sin I_s$. Since the orbital axis of a transiting planet must be nearly perpendicular to the line-of-sight ($\sin I_o \approx 1$), a small value of $\sin I_s$ implies a spin-orbit misalignment.

The pioneering analysis of Schlaufman (2010) was based on spectroscopic determinations of $V \sin I_s$, as well as statistical estimates of V based on the rotation-age-mass correlations that are observed for main-sequence stars. It is also possible to measure V more directly, if accurate estimates of the stellar radius R_s and rotation period P_s are available, using the relation $V = 2\pi R_s / P_s$ (see, e.g., Doyle et al. 1984). It has also become possible to estimate $\sin I_s$ using asteroseismology (e.g., Chaplin et al. 2013).

An important advantage of this technique is that the difficulty of measuring stellar inclinations is independent of the size of the transiting planet, and therefore the spin-orbit relation may be investigated even for smaller planets (such as Earth-sized planets). One shortcoming

Electronic address: hirano@geo.titech.ac.jp

¹ Department of Earth and Planetary Sciences, Tokyo Institute of Technology, 2-12-1 Ookayama, Meguro-ku, Tokyo 152-8551, Japan

² Department of Physics, and Kavli Institute for Astrophysics and Space Research, Massachusetts Institute of Technology, Cambridge, MA 02139

³ National Astronomical Observatory of Japan, 2-21-1 Osawa, Mitaka, Tokyo, 181-8588, Japan

⁴ Department of Astronomy, The University of Tokyo, Tokyo, 113-0033, Japan

of this technique is that the relative uncertainty in I_s becomes large when I_s approaches 90° . Another is that it is often difficult to obtain accurate and precise measurements of $V \sin I_s$ for cool stars ($T_{\text{eff}} < 6000$ K), for which the rotational line broadening is often comparable to the effects of instrumental broadening and macroturbulence. This is contrast with measurements of the RM effect, by which the sky-projected spin-orbit angle λ can often be measured to within 5-10 degrees (e.g., Triaud et al. 2010; Hirano et al. 2011a). For these reasons, it may be best to regard this technique as an efficient method for identifying low-inclination hot stars; and for identifying *candidate* low-inclination cool stars that can be followed up with complementary techniques.

In the precursor to this paper, Hirano et al. (2012a) determined stellar inclinations for 7 host stars of transiting-planet candidates. To measure rotation periods P_s , they used a periodogram analysis of the light curve modulations seen with the *Kepler* telescope. They also undertook new spectroscopic measurements of $V \sin I_s$ and stellar radii R_s via $I_s = \arcsin(P_s \cdot V \sin I_s / 2\pi R_s)$, for several KOIs (Kepler Objects of Interest). They found that most of the systems are consistent with $I_s = 90^\circ$, suggesting good spin-orbit alignment, but at least one system (KOI-261) may have a spin-orbit misalignment. The planet Kepler-63b was also found to have a tilted orbit using the same technique, and also through the measurement of the sky-projected obliquity using the RM effect (Sanchis-Ojeda et al. 2013). More recently, Walkowicz & Basri (2013) applied the same technique and found candidate spin-orbit misalignments for several KOI's including a multiple transiting system (Kepler-9). Even more recently, a robust spin-orbit misalignment around multiple systems was reported for Kepler-56 based on the asteroseismic determination of the stellar inclination (Huber et al. 2013).

In this paper, we continue the effort by Hirano et al. (2012a) to examine the stellar inclinations for KOI systems. In the next section, we describe the new spectroscopic observations with the Subaru telescope to obtain basic spectroscopic parameters for 25 KOI systems, including 10 systems with multiple transiting planets. We then present the analyses of stellar rotational periods and spectroscopic parameters such as $V \sin I_s$ and R_s in Section 3. Section 4 presents a statistical analysis of the observed distribution of I_s . We try to test some hypotheses such as whether the observed values of I_s are drawn from an isotropic distribution (§4.3). Section 5 summarizes our results and their implications.

2. TARGET SELECTION AND OBSERVATIONS

We composed a list of KOIs for measurements of stellar inclinations based on the following criteria: (1) a preliminary light curve analysis shows a peak power in the Lomb-Scargle periodogram larger than 1000, (2) the estimated rotation velocity at the stellar equator is larger than about 3 km s^{-1} , and (3) the apparent magnitude in the *Kepler* bandpass is $m_{\text{Kep}} \lesssim 14$. The rotational velocity needed for the second criterion was estimated from the stellar radius in the Kepler Input Catalog (KIC) and the preliminary estimate of the rotation period. We excluded slow rotators because the measurement of $V \sin I_s$ for slow rotators ($V \sin I_s \lesssim 3 \text{ km s}^{-1}$) has a large fractional uncertainty, as shown below.

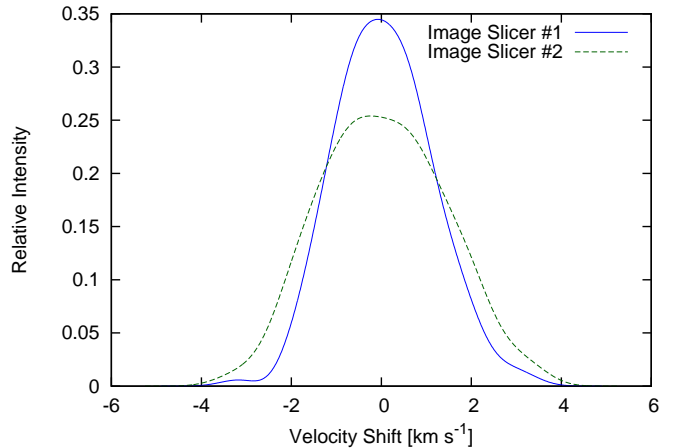


FIG. 1.— Instrumental profiles of Subaru/HDS for Image Slicer #1 (blue solid line) and #2 (green dashed line). These profiles were extracted from the same spectral region that was used to determine the $V \sin I_s$ of the program stars.

In order to estimate the basic spectroscopic parameters, we conducted high dispersion spectroscopy with Subaru/HDS on 2012 June 30, July 1, 2, and September 4; and on 2013 June 20 and 21. All together we obtained spectra for 25 KOIs. During the 2012 observations, we employed the standard “I2a” setup with Image Slicer #1 (Tajitsu et al. 2012), attaining a spectral resolution of $R \sim 110,000$. For the 2013 observations we used Image Slicer #2 ($R \sim 80,000$). On each night of observations, we obtained a spectrum of the flat-field lamp through the iodine cell, to determine the instrumental line broadening function. In the subsequent analysis, the line broadening due to the instrumental profile (IP) for each setup was deconvolved as shown in Figure 1, and taken into account when we estimated the rotation velocity of each star.

Each spectrum was subjected to standard IRAF procedures to extract a one-dimensional (1D) spectrum. The wavelength scale was set with reference to a spectrum of the thorium-argon lamp. The resultant signal-to-noise ratio (SNR) in the 1D spectrum was typically $50\text{--}100 \text{ pixel}^{-1}$. The I2a setup covers the spectral region between $4900\text{--}7600 \text{ \AA}$, within which there is a large number of iron lines available for estimation of the photospheric parameters.

3. ANALYSES AND RESULTS

3.1. Estimate for Rotation Periods

We determined the rotation periods of the stars using the photometric observations provided by the *Kepler* telescope (Borucki et al. 2010). In particular, we used the Long Cadence data (30 minute integrations) available from the MAST archive from quarters 2 through 16, for up to a total of approximately 4 years of data. Previously, Hirano et al. (2012a) used the simple aperture flux data to obtain the rotation periods, but those data needed to be treated carefully to remove systematic and instrumental effects on timescales similar to the rotation periods. In this paper we used the PDC-MAP final data product, since it is designed to remove the unphysical trends leaving the signal of stellar spots unaltered (Smith et al. 2012; Stumpe et al. 2012).

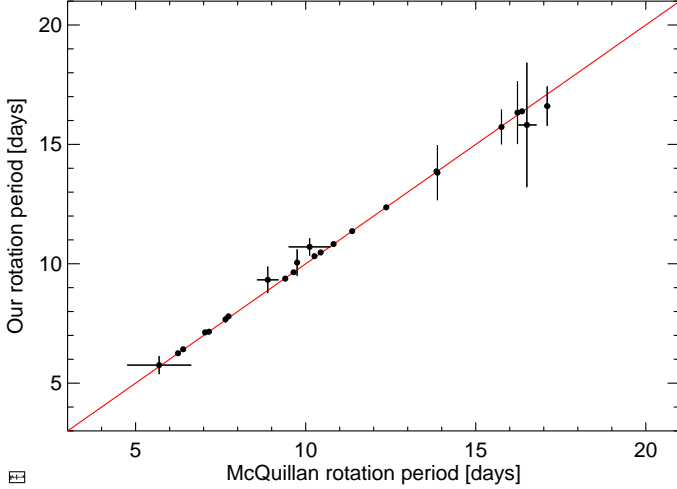


FIG. 2.— Comparison between the rotation periods listed in Table 1 and periods estimated by McQuillan et al. (2013b).

To excise the data obtained during transits, we identified the transit intervals using the publicly available transit ephemerides (Batalha et al. 2013) downloaded from the NASA exoplanet archive (Akeson et al. 2013), which are based on the assumption of constant orbital periods. We also removed gross outliers, and normalized the data from each quarter by dividing by the quarterly median flux. We then computed the Lomb-Scargle periodogram adopting the definition and algorithm described by Press & Rybicki (1989). In general each periodogram showed several peaks, the strongest of which can be attributed to stellar variability. We selected the strongest peak of the periodogram as the first candidate for the rotation period, and adopted the full width at half maximum (FWHM) of the peak as the 1σ uncertainty. We also performed a visual inspection of each light curve to make sure that the stellar flux appeared to be varying quasi-periodically with the candidate rotation period, as opposed to a more regular periodic signal that would be caused by orbital effects or pulsation. In particular, we looked for quasi-sinusoidal variations with slow amplitude and phase modulation on a timescale of a few rotation periods, as would be expected of starspots. We also checked that there was not additional power at twice the candidate rotation period, as it sometimes happens when a star has two similar size starspots in opposite longitudes. Such a configuration causes the flux variations to peak twice per rotation period, inducing a substitute for a subharmonic peak at half the rotation period, which in some occasions could be more significant than the real rotation period peak, making our code identify the wrong rotation period. In two cases, KOI-180 and KOI-2636, the strongest peak corresponded to half the rotation period, so we matched the correct peak with the rotation period, and assigned the right uncertainty neglecting all the power at half the rotation period. Table 1 summarizes our rotation period measurements, including the peak value of the periodogram power and the variability amplitude, defined as the full range of flux after eliminating the lowest 10% and the highest 10% of the flux values (Hirano et al. 2012a).

McQuillan et al. (2013a) advocated the autocorrelation function, rather than the Lomb-Scargle peri-

TABLE 1
ROTATION PERIODS ESTIMATED FROM THE *Kepler* PHOTOMETRY.
ALSO GIVEN ARE THE PEAK PERIODOGRAM POWER AND THE
VARIABILITY AMPLITUDE (DEFINED AS IN THE TEXT).

System	P_s (days)	Peak Power	Variability Amplitude (%)
KOI-180	15.728 ± 0.726	3266.21	0.348
KOI-285	16.829 ± 0.588	1474.14	0.013
KOI-304	15.814 ± 2.606	1470.75	0.070
KOI-323	7.674 ± 0.143	4121.72	0.566
KOI-635	9.328 ± 0.558	1814.23	0.142
KOI-678	13.871 ± 0.058	14941.34	0.924
KOI-718	16.603 ± 0.828	1225.87	0.045
KOI-720	9.378 ± 0.027	7967.45	0.670
KOI-988	12.363 ± 0.064	15540.17	0.685
KOI-1615	7.797 ± 0.043	5516.86	0.256
KOI-1628	5.756 ± 0.378	2540.79	0.179
KOI-1779	7.154 ± 0.014	9393.85	0.548
KOI-1781	10.474 ± 0.084	7000.01	0.733
KOI-1797	10.826 ± 0.033	14184.33	0.679
KOI-1835	9.644 ± 0.028	11825.34	0.531
KOI-1839	6.252 ± 0.027	8156.72	0.810
KOI-1890	6.420 ± 0.039	2716.78	0.020
KOI-1916	10.318 ± 0.097	3128.06	0.144
KOI-2001	16.385 ± 0.081	14017.50	0.843
KOI-2002	10.708 ± 0.364	1989.29	0.138
KOI-2026	10.051 ± 0.555	2530.09	0.191
KOI-2035	7.127 ± 0.104	7347.71	0.741
KOI-2087	13.816 ± 1.155	1902.26	0.086
KOI-2261	11.366 ± 0.042	17009.04	0.515
KOI-2636	16.330 ± 1.317	1774.31	0.077

odogram, for measuring rotation periods with *Kepler* data. We checked our measured rotation periods against a published table of rotation periods that were determined using the autocorrelation function (McQuillan et al. 2013b), and found good agreement between the results of both techniques (Figure 2), although our quoted uncertainties are always larger.

3.2. Spectroscopic Parameters

3.2.1. Photospheric Parameters, and Stellar Radius

Based on Takeda et al. (2002, 2005), we estimated the basic photospheric parameters (the effective temperature T_{eff} , surface gravity $\log g$, microturbulent velocity ξ , and metallicity $[\text{Fe}/\text{H}]$) by measuring the equivalent widths of the available iron absorption lines. That is, these parameters are established by requiring that the following three conditions are simultaneously fulfilled: (a) excitation equilibrium (Fe abundances show no systematic dependence on the excitation potential), (b) ionization equilibrium (mean Fe abundance from Fe I lines and that from Fe II lines agree with each other), and (c) curve-of-growth matching (Fe abundances do not systematically depend on line strengths). We used typically ~ 150 – 200 and ~ 10 – 15 lines for Fe I and Fe II, respectively.

We next convert the photospheric parameters into stellar masses and radii employing the Yonsei-Yale (Y^2) stellar-evolutionary models (Yi et al. 2001). Since an accurate estimation of the stellar radius is essential in our methodology, it is important to take account of the accuracy of the photospheric parameters. Bruntt et al. (2010) spectroscopically analyzed 23 solar-type stars, arguing that the “true” effective temperature of a star defined from the stellar luminosity and radius might have a systematic offset of -40 ± 20 K from the spectroscopic model parameter T_{eff} , while spectroscopic measurements

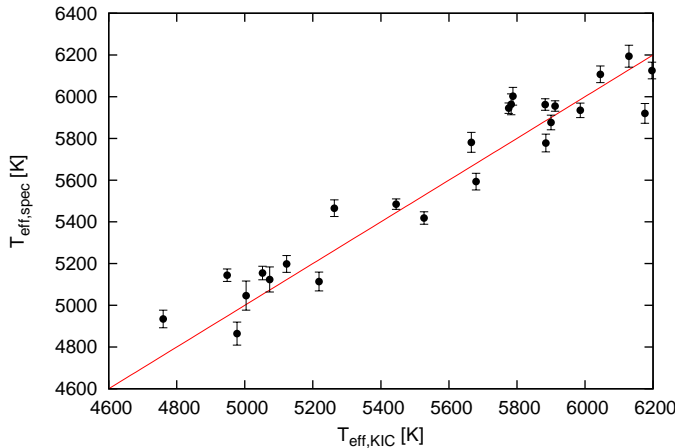


FIG. 3.— Comparison between our measurement of T_{eff} , and the value of T_{eff} reported in the Kepler Input Catalog (KIC).

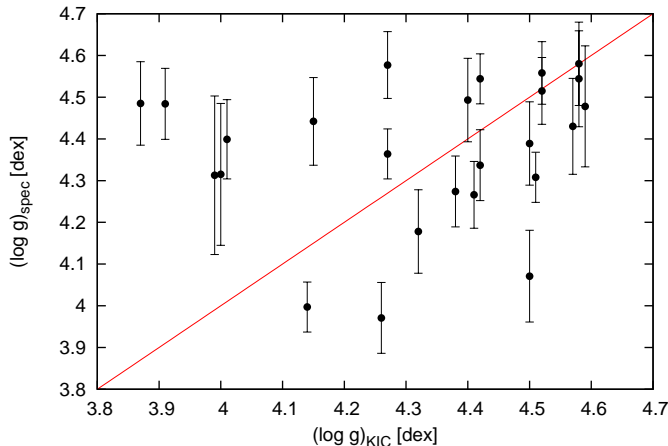


FIG. 4.— Comparison between our measurement of $\log g$ and the KIC value of $\log g$. While both quantities are in good agreement for $\log g \gtrsim 4.3$ dex, large discrepancies are seen for smaller value of $\log g$.

of the surface gravity $\log g$ did not show a significant offset. Since our spectroscopic measurement of T_{eff} is similar to that of Bruntt et al. (2010), we assume that the systematic error in T_{eff} is 40 K, which is quadratically added to the internal statistical error listed in Table 2 when we estimate the stellar radii and masses based with the Y^2 isochrones. To account for these uncertainties (both statistic and systematic) in the photospheric parameters, we randomly generated many sets of $(T_{\text{eff}}, \log g, \text{ and } [\text{Fe}/\text{H}])$ assuming Gaussian distributions for their uncertainties. Each set of $(T_{\text{eff}}, \log g, \text{ and } [\text{Fe}/\text{H}])$ was then converted to the mass and radius on the Y^2 isochrones. The resultant distributions give the estimates (and errors) for the mass and radius of each system. Table 2 summarizes our measurements of the photospheric parameters together with the stellar radius.

To check whether our spectroscopically-derived photospheric parameters are compatible with the parameters that were determined from broadband photometry, we compared our effective temperatures and surface gravities with the values reported in the Kepler In-

put Catalog (KIC). Figures 3 and 4 show these comparisons. The root-mean-squared residual between the spectroscopic and photometric T_{eff} and $\log g$ are 124 K and 0.26 dex, respectively. This level of agreement seems reasonable given the relatively large uncertainties in the KIC parameters (~ 200 K for T_{eff} and ~ 0.4 dex for $\log g$, Brown et al. 2011).

3.2.2. Projected Rotational Velocity

We measured the projected rotational velocity $V \sin I_s$ by fitting a model to the observed spectrum for each system. Theoretically, an observed stellar spectrum $I_{\text{obs}}(\lambda)$ can be considered as the convolution of several functions:

$$I_{\text{obs}}(\lambda) = S(\lambda) * M(\lambda) * \text{IP}, \quad (1)$$

where $S(\lambda)$ is the intrinsic stellar spectrum taking into account only thermal and natural broadening (including microturbulence), $M(\lambda)$ is the broadening kernel representing rotation and macroturbulence (Gray 2005), and IP represents the instrumental line profile (see Figure 1). The IP was determined by deconvolving the spectrum of the flat-field lamp through the iodine cell. For each target star, we generated the intrinsic spectrum $S(\lambda)$ based on the ATLAS9 model (a plane-parallel stellar atmosphere model in LTE, Kurucz 1993) with the input photospheric parameters being the best-fit values derived above, and fitted the observed spectrum $I_{\text{obs}}(\lambda)$, allowing $V \sin I_s$ to be a free parameter (which affects $M(\lambda)$). As for the macroturbulence, we adopted the radial-tangential model of Gray (2005) and assumed that the macroturbulent velocity ζ_{RT} is expressed by the following empirical formula (Valenti & Fischer 2005):

$$\zeta_{\text{RT}} = \left(3.98 + \frac{T_{\text{eff}} - 5770 \text{ K}}{650 \text{ K}} \right) \text{ km s}^{-1}. \quad (2)$$

This empirical formula was derived based on the statistical distribution of the upper limit of ζ_{RT} , in which $V \sin I_s = 0 \text{ km s}^{-1}$ was assumed in fitting the spectral lines for a large number of stars in the controlled sample (the SPOCS catalog). Taking the “lower” boundary of the upper limit of ζ_{RT} as a function of T_{eff} , Valenti & Fischer (2005) derived Equation (2) (see Figure 3 in Valenti & Fischer 2005). In the subsequent analysis we assumed that the uncertainty in ζ_{RT} is $\pm 15\%$ for cool stars ($T_{\text{eff}} \leq 6100 \text{ K}$) based on the observed dispersion of the upper limit of ζ_{RT} around Equation (2). But for hot stars ($> 6100 \text{ K}$) for which the SPOCS catalog has a relatively small number of stars, we conservatively adopted $\pm 25\%$ for the systematic uncertainty in ζ_{RT} .

3.2.3. Correction for the Impact of Differential Rotation

The Sun’s rotation period varies with surface latitude; the rotation rate at the Sun’s equator is faster than that of the polar region by about 20%. It is natural to assume that differential rotation is a feature of all our program stars, and therefore that differential rotation needs to be taken into account in our analysis.

As pointed out by Hirano et al. (2012a), there are two main issues that arise because of differential rotation. The first issue is that we do not know the latitude of the spots that are producing the detectable photometric variations. Starspots are probably not randomly distributed;

TABLE 2

SPECTROSCOPIC PARAMETERS. STARRED SYSTEMS ARE MULTIPLE TRANSITING SYSTEMS. WE SHOW $\sin I_s \equiv V \sin I_s / V_{\text{eq}}$ IN THE RIGHTMOST COLUMN BASED ON THE VALUES OF V_{eq} AND $V \sin I_s$. THE LISTED ERRORS IN T_{eff} REPRESENT THE INTERNAL STATISTICAL ERROR AND DO NOT INCLUDE THE SYSTEMATIC ERROR (SEE SECTION 3.2.1).

System	T_{eff} (K)	$\log g$	[Fe/H]	M_s (M_{\odot})	R_s (R_{\odot})	$V \sin I_s$ (km s $^{-1}$)	V_{eq} (km s $^{-1}$)	$\sin I_s$
KOI-180	5592 \pm 40	4.389 \pm 0.100	0.12 \pm 0.05	0.992 $^{+0.027}_{-0.022}$	1.029 $^{+0.077}_{-0.088}$	3.15 \pm 0.81	3.30 $^{+0.45}_{-0.31}$	0.941 $^{+0.276}_{-0.255}$
KOI-285	5962 \pm 27	3.997 \pm 0.060	0.16 \pm 0.03	1.324 $^{+0.047}_{-0.051}$	1.914 $^{+0.134}_{-0.145}$	4.21 \pm 0.77	5.74 $^{+1.28}_{-0.59}$	0.708 $^{+0.180}_{-0.162}$
KOI-304*	5777 \pm 42	4.399 \pm 0.095	-0.14 \pm 0.05	0.962 $^{+0.026}_{-0.022}$	1.009 $^{+0.068}_{-0.086}$	1.62 \pm 1.28	3.22 $^{+0.84}_{-0.53}$	0.484 $^{+0.425}_{-0.383}$
KOI-323	5418 \pm 30	4.558 \pm 0.075	0.01 \pm 0.04	0.927 $^{+0.021}_{-0.026}$	0.841 $^{+0.054}_{-0.030}$	4.70 \pm 0.30	5.56 $^{+0.39}_{-0.24}$	0.838 $^{+0.072}_{-0.071}$
KOI-635	6194 \pm 52	4.493 \pm 0.100	0.25 \pm 0.07	1.260 $^{+0.026}_{-0.031}$	1.173 $^{+0.050}_{-0.040}$	8.82 \pm 0.52	6.39 $^{+1.08}_{-0.54}$	1.360 $^{+0.172}_{-0.194}$
KOI-678*	5129 \pm 32	4.532 \pm 0.085	0.19 \pm 0.04	0.886 $^{+0.023}_{-0.018}$	0.833 $^{+0.031}_{-0.046}$	3.21 \pm 0.45	3.04 $^{+0.16}_{-0.18}$	1.058 $^{+0.164}_{-0.157}$
KOI-718*	6002 \pm 42	4.577 \pm 0.080	0.58 \pm 0.04	1.215 $^{+0.028}_{-0.022}$	1.133 $^{+0.049}_{-0.044}$	2.53 \pm 1.26	3.45 $^{+0.80}_{-0.31}$	0.697 $^{+0.382}_{-0.351}$
KOI-720*	5198 \pm 40	4.580 \pm 0.100	0.01 \pm 0.05	0.862 $^{+0.023}_{-0.020}$	0.789 $^{+0.040}_{-0.038}$	4.18 \pm 0.30	4.25 $^{+0.25}_{-0.20}$	0.980 $^{+0.091}_{-0.087}$
KOI-988*	5114 \pm 45	4.544 \pm 0.115	0.10 \pm 0.04	0.861 $^{+0.022}_{-0.019}$	0.802 $^{+0.032}_{-0.045}$	2.64 \pm 0.57	3.28 $^{+0.17}_{-0.19}$	0.808 $^{+0.181}_{-0.177}$
KOI-1615	5934 \pm 35	4.266 \pm 0.080	0.21 \pm 0.04	1.181 $^{+0.055}_{-0.038}$	1.321 $^{+0.161}_{-0.135}$	8.74 \pm 0.21	8.57 $^{+1.24}_{-0.91}$	1.017 $^{+0.127}_{-0.128}$
KOI-1628	6125 \pm 40	4.274 \pm 0.085	0.13 \pm 0.04	1.218 $^{+0.050}_{-0.033}$	1.328 $^{+0.168}_{-0.137}$	11.24 \pm 0.27	11.71 $^{+1.90}_{-1.42}$	0.957 $^{+0.137}_{-0.133}$
KOI-1779*	5781 \pm 47	4.442 \pm 0.105	0.33 \pm 0.07	1.124 $^{+0.027}_{-0.024}$	1.058 $^{+0.133}_{-0.049}$	7.41 \pm 0.24	7.48 $^{+1.03}_{-0.38}$	0.979 $^{+0.073}_{-0.112}$
KOI-1781*	4864 \pm 55	4.478 \pm 0.145	0.19 \pm 0.06	0.815 $^{+0.020}_{-0.018}$	0.766 $^{+0.028}_{-0.034}$	3.64 \pm 0.22	3.67 $^{+0.15}_{-0.17}$	0.994 $^{+0.077}_{-0.072}$
KOI-1797	4934 \pm 42	4.430 \pm 0.115	0.16 \pm 0.06	0.824 $^{+0.017}_{-0.015}$	0.781 $^{+0.025}_{-0.028}$	3.69 \pm 0.23	3.65 $^{+0.14}_{-0.13}$	1.011 $^{+0.075}_{-0.072}$
KOI-1835*	5046 \pm 70	4.313 \pm 0.190	0.16 \pm 0.07	0.862 $^{+0.264}_{-0.026}$	0.832 $^{+1.216}_{-0.041}$	4.66 \pm 0.20	4.36 $^{+6.39}_{-0.21}$	1.012 $^{+0.126}_{-0.580}$
KOI-1839	5465 \pm 40	4.485 \pm 0.100	0.05 \pm 0.06	0.938 $^{+0.028}_{-0.022}$	0.908 $^{+0.051}_{-0.062}$	7.41 \pm 0.15	7.35 $^{+0.46}_{-0.51}$	1.010 $^{+0.077}_{-0.064}$
KOI-1890	6107 \pm 40	3.971 \pm 0.085	0.22 \pm 0.05	1.477 $^{+0.094}_{-0.084}$	2.078 $^{+0.285}_{-0.247}$	7.44 \pm 0.49	16.38 $^{+2.61}_{-2.00}$	0.452 $^{+0.073}_{-0.066}$
KOI-1916*	5945 \pm 25	4.308 \pm 0.060	0.31 \pm 0.04	1.193 $^{+0.034}_{-0.025}$	1.265 $^{+0.109}_{-0.094}$	6.38 \pm 0.39	6.20 $^{+0.86}_{-0.52}$	1.017 $^{+0.125}_{-0.128}$
KOI-2001	5144 \pm 30	4.484 \pm 0.085	0.01 \pm 0.04	0.839 $^{+0.016}_{-0.014}$	0.804 $^{+0.021}_{-0.029}$	2.44 \pm 0.66	2.48 $^{+0.13}_{-0.10}$	0.980 $^{+0.272}_{-0.268}$
KOI-2002	5963 \pm 50	4.071 \pm 0.110	0.15 \pm 0.05	1.342 $^{+0.083}_{-0.080}$	1.776 $^{+0.273}_{-0.263}$	5.67 \pm 0.42	8.39 $^{+1.64}_{-1.30}$	0.671 $^{+0.140}_{-0.116}$
KOI-2026	5919 \pm 47	4.178 \pm 0.100	0.01 \pm 0.05	1.106 $^{+0.060}_{-0.041}$	1.419 $^{+0.200}_{-0.175}$	4.76 \pm 0.50	7.15 $^{+1.32}_{-0.98}$	0.659 $^{+0.136}_{-0.116}$
KOI-2035	5484 \pm 25	4.544 \pm 0.060	0.13 \pm 0.04	0.984 $^{+0.021}_{-0.023}$	0.885 $^{+0.047}_{-0.024}$	6.35 \pm 0.21	6.30 $^{+0.39}_{-0.22}$	1.002 $^{+0.055}_{-0.061}$
KOI-2087	5955 \pm 25	4.364 \pm 0.060	0.02 \pm 0.03	1.084 $^{+0.024}_{-0.020}$	1.129 $^{+0.087}_{-0.075}$	4.46 \pm 0.73	4.15 $^{+0.83}_{-0.47}$	1.048 $^{+0.250}_{-0.221}$
KOI-2261*	5154 \pm 32	4.515 \pm 0.080	0.12 \pm 0.05	0.873 $^{+0.021}_{-0.016}$	0.830 $^{+0.027}_{-0.042}$	2.81 \pm 0.55	3.69 $^{+0.17}_{-0.19}$	0.764 $^{+0.156}_{-0.153}$
KOI-2636	5876 \pm 35	4.337 \pm 0.085	0.16 \pm 0.04	1.118 $^{+0.037}_{-0.027}$	1.181 $^{+0.145}_{-0.114}$	2.40 \pm 1.26	3.67 $^{+0.84}_{-0.47}$	0.631 $^{+0.372}_{-0.336}$

they are likely to be concentrated around particular latitudes. On the Sun, the “active latitudes” gradually vary from about $\pm 40^\circ$ down to the equator, over the 11-year solar cycle. Therefore, we need to take account the systematic errors due to the imperfect knowledge of the spots’ locations. The second issue is the distortion in the spectral line shape caused by differential rotation. The absorption lines of a Sun-like star are narrower than would be expected for a star with no differential rotation, because differential rotation reduces the weight of the extremes in rotation velocity. Therefore, an analysis of spectral lines that neglects differential rotation will give a value of $V \sin I_s$ that is systematically smaller than the true equatorial projected rotation velocity.

We corrected for the first of these two issues using the procedure described by Hirano et al. (2012a). Employing the empirical relation given by Collier Cameron (2007) for the magnitude of differential rotation, we express the rotation rate Ω as a function of the latitude l on the stellar surface:

$$\Omega(l) = \Omega_{\text{eq}}(1 - \alpha \sin^2 l), \quad (3)$$

where Ω_{eq} is the angular rotation velocity at the equator, and

$$\alpha \Omega_{\text{eq}} = 0.053 \left(\frac{T_{\text{eff}}}{5130 \text{ K}} \right)^{8.6} \text{ rad day}^{-1}. \quad (4)$$

Assuming that the observed rotation rates are due to spots located at the stellar latitude $l = 20^\circ \pm 20^\circ$ (as is the case for the Sun), we re-estimated the equatorial rotation velocity (V_{eq}) for each of the targets as

$$V_{\text{eq}} = \frac{2\pi R_s}{P_s} \frac{1}{1 - \alpha \sin^2 20^\circ}, \quad (5)$$

and added in quadrature the following lower and upper systematic errors in V_{eq} :

$$(\Delta V_{\text{eq}})_{\text{low,sys}} = V_{\text{eq}} \left(\frac{1}{1 - \alpha \sin^2 20^\circ} - 1 \right), \quad (6)$$

$$(\Delta V_{\text{eq}})_{\text{upp,sys}} = V_{\text{eq}} \left(\frac{1}{1 - \alpha \sin^2 40^\circ} - \frac{1}{1 - \alpha \sin^2 20^\circ} \right). \quad (7)$$

Table 2 gives the resulting estimates of the equatorial rotation velocities. For reference, the assumed magnitude of differential rotation was on average $\alpha \simeq 0.23$ for the targets listed in Table 2, which is nearly the same as that of the Sun.

Regarding the second issue, the bias in the $V \sin I_s$ measurement, we performed a correction using the following procedure. First, we computed $\sin I_s$ for each target based on the preliminary measurements of $V \sin I_s$ and V_{eq} (before any correction to $V \sin I_s$ for differential rotation). A simulated line profile was then generated, using the model of Equation (1). In this case $M(\lambda)$ corresponds to the macroturbulence-plus-rotation kernel in the presence of differential rotation using $\sin I_s$, V_{eq} , and α as input parameters. We adopted plausible values for the other spectroscopic parameters (i.e., the intrinsic Gaussian and Lorentzian dispersions, macroturbulence, limb-darkening, and IP) in making the mock profile. This mock line was then fitted assuming zero differential rotation, with $V \sin I_s$ as the only free parameter. After computing the ratio f of the resultant best-fitting $V \sin I_s$ to the product of the input V_{eq} and $\sin I_s$, we divided the originally measured $V \sin I_s$ by the ratio f to obtain the final $V \sin I_s$ corrected for the impact of differential rotation. We note that $f \approx 1 - \alpha/2$

was in general obtained, indicating that the measured $V \sin I_s$ is always underestimated when a rigid rotation is assumed in fitting the spectrum (also see Figure 11 in Hirano et al. 2012a). The resultant $V \sin I_s$ after the correction of differential rotation for each system is also summarized in Table 2.

Some of our program stars were also studied by Walkowicz & Basri (2013), giving us the opportunity to check on the agreement. For the stars KOI-180, 323, and 988, respectively, Walkowicz & Basri (2013) found $V \sin I_s = 2.7 \pm 0.5 \text{ km s}^{-1}$, $3.3 \pm 0.5 \text{ km s}^{-1}$, and $2.7 \pm 0.5 \text{ km s}^{-1}$. Comparing these with the values in Table 2, KOI-180 and 988 show a good agreement between two measurements, but KOI-323 shows a $\sim 3\sigma$ level disagreement. Furthermore, for KOI-261, Walkowicz & Basri (2013) found $V \sin I_s = 2.3 \pm 0.5 \text{ km s}^{-1}$, which is in agreement with the 1σ upper limit of 2.57 km s^{-1} determined by Hirano et al. (2012a) using the same technique as applied here.

4. DISCUSSION

4.1. Evidence of Spin-orbit Misalignment

Figure 5 plots $V \sin I_s$ against V_{eq} , after making the corrections for differential rotation. Single transiting systems are shown in panel (a), and systems with multiple transiting candidates are shown in panel (b). The black solid line represents $I_s = 90^\circ$. Systems falling on this line would have the stellar spin oriented perpendicular to the line-of-sight, and therefore likely aligned with the planetary orbital axes (although an unlikely possibility is that they are misaligned with the line of nodes coincidentally along the line of sight). The dashed lines show different degrees of misalignment ($I_s = 45^\circ$ and $I_s = 30^\circ$).

Most of the data points in Figure 5 do indeed fall near the $I_s = 90^\circ$ line, indicating a tendency toward spin-orbit alignment. Four of the systems—KOI-323, 1890, 2002, and 2026—show evidence for significant spin-orbit misalignments with more than 2σ confidence. All four of these systems are single-transiting candidates. Some of the multiple-transiting candidates also show evidence for misalignment but only at the 1σ level; these are KOI-304, 988, and 2261.

As the multiple-transiting systems are of special importance, it is worth focusing on those possible misalignments and check if the results for the rotation period, stellar radius, and $V \sin I_s$ are robust. A spurious finding of misalignment can result from an underestimate of either $V \sin I_s$ or P , or an overestimate of R_s .

First, we check on the rotation periods. The relevant light curves and periodograms are shown in Figure 6. Each light curve shown in Figure 6 shows an evident pattern of quasi-periodic flux variation, and the periodograms for KOI-988 and KOI-2261 exhibit a clear and unambiguous peak that surpasses a power of 10^4 . For the case of KOI-304, on the other hand, there are multiple, relatively weak peaks of comparable power. These multiple peaks could be ascribed to differential rotation or rapid starspot evolution. Nevertheless, visual inspection of the light curves does not reveal any problem with the quoted rotation periods of 15.8 ± 2.6 days for KOI-304.

Next, we check on the determination of the stellar radius. We have already shown in Section 3.2.1 that the photospheric parameters (T_{eff} and $\log g$) are in reasonably good agreement with the KIC values. Here we fo-

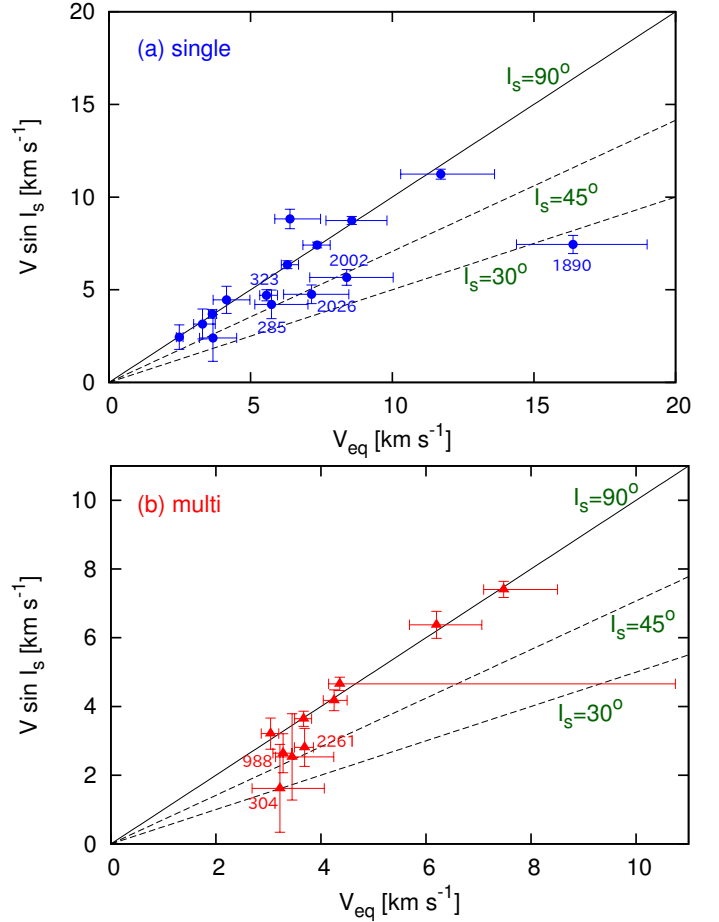


FIG. 5.— Projected rotational velocity ($V \sin I_s$) as a function of the stellar rotation velocity at the equator (V_{eq}), for (a) single and (b) multiple KOI systems. We plot here the newly observed 25 KOI systems. The solid lines indicate $I_s = 90^\circ$ while the dashed lines represent different degrees of misalignment ($I_s = 30^\circ$ and $I_s = 45^\circ$). In the lower panel, the data point with the very large upper uncertainty in V_{eq} is KOI-1835, which has a poorly determined surface gravity (and thus a poorly determined stellar radius). Note that the panels (a) and (b) show different ranges of V_{eq} .

cus on the estimate of stellar mass and radius, based on the Y^2 isochrones. Figure 7 shows the placement of the measured values of T_{eff} and $\log g$ (red crosses) on the theoretical isochrones (blue dashed lines) and the loci of equal stellar radius (black solid lines) of the Y^2 theoretical evolutionary models for main-sequence stars. The measured values of T_{eff} and $\log g$ for KOI-304, 988, and 2261 conform with the models.

Finally, we check on the measurements of $V \sin I_s$ based on the observed line broadening in the Subaru spectra. Figure 8 shows part of the observed spectrum (blue dots) along with the best-fitting model spectrum (red line) for each of (a) KOI-304, (b) KOI-988, and (c) KOI-2261. For reference, the green area shows the spectral lines that would be expected for $\sin I_s = 1$ (i.e., spin-orbit alignment). The breadth of the green area arises from variation of the macroturbulent velocity ζ_{RT} by $\pm 15\%$ from the value computed by Equation (2). A misaligned system will show narrower lines than the green region. This figure illustrates the main difficulty of this probe of spin-orbit alignment: one must isolate the very

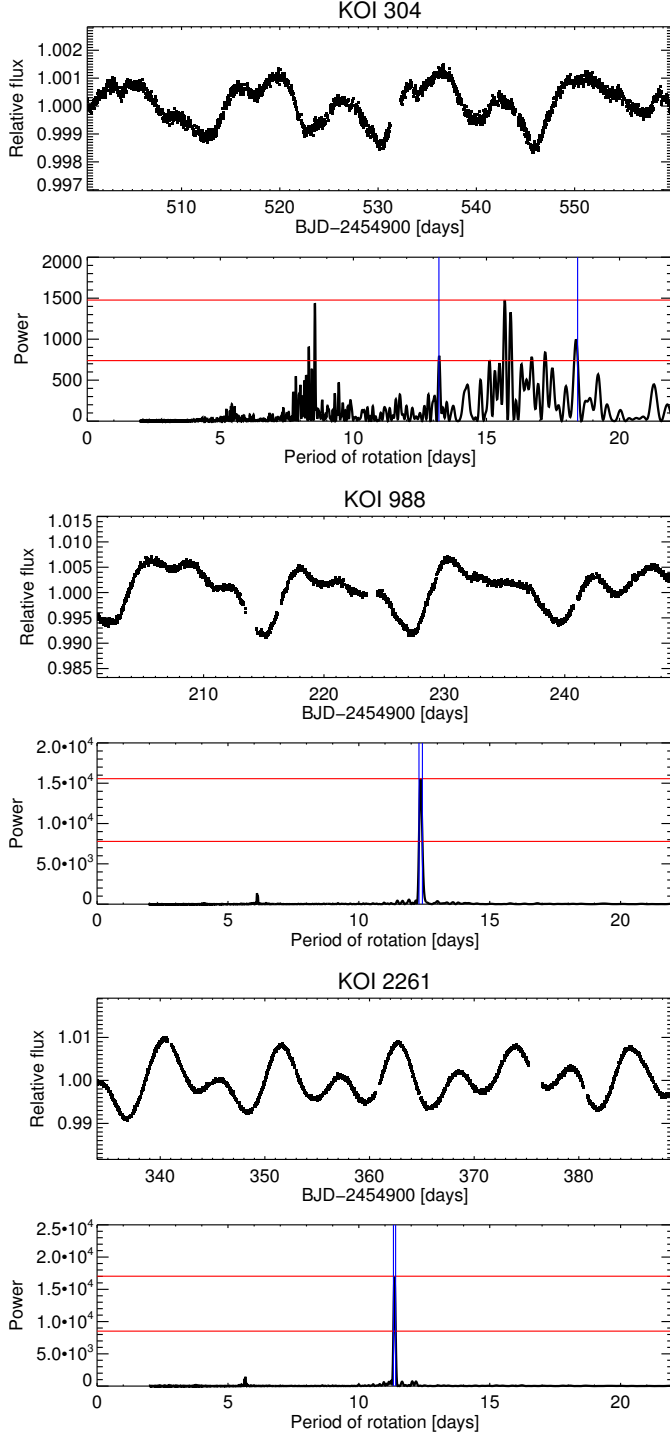


FIG. 6.— Light curves and Lomb-Scargle periodograms for multi-planet systems showing a possible spin-orbit misalignment (KOI-304, 988, 2261). In the periodograms, the intervals surrounded by the two blue lines correspond to the rotation periods and their uncertainties (§3.1).

small differences in line broadening due to rotation as opposed to macroturbulence and instrumental broadening. For all the three systems shown here, $V \sin I_s$ cannot be much larger than the values listed in Table 2 (see in particular the bottom of each absorption line), unless the assumed macroturbulent velocity is in error by more than 15%. It is important to remember that Figure 8 shows

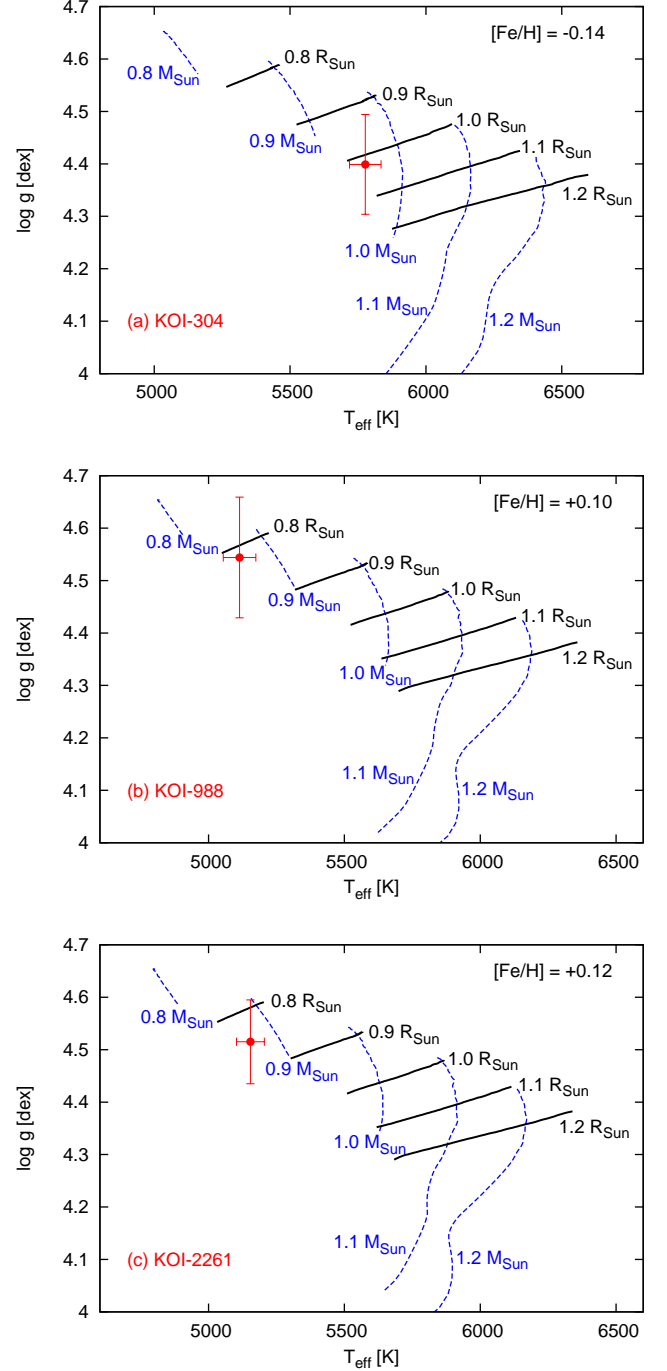


FIG. 7.— Placements of measured T_{eff} and $\log g$ in the Y^2 isochrone for (a) KOI-304, (b) KOI-988, and (c) KOI-2261 (red crosses with error bars). The blue dashed lines indicate the evolutionary tracks and the black solid lines are the “iso-radius”, based on the Y^2 isochrone. Note that the errorbars in T_{eff} are enlarged so that they contain the systematic error of 40 K.

only a part of the observed spectrum. The true statistical significance of the results is higher than it might seem visually because $V \sin I_s$ was determined from data over a wider range of wavelengths.

In summary, the detailed visual inspection of the multi-transiting systems with possible misalignments did not raise any specific concerns for all of KOI-304, 988, and 2261, which remain viable candidates for multi-planet

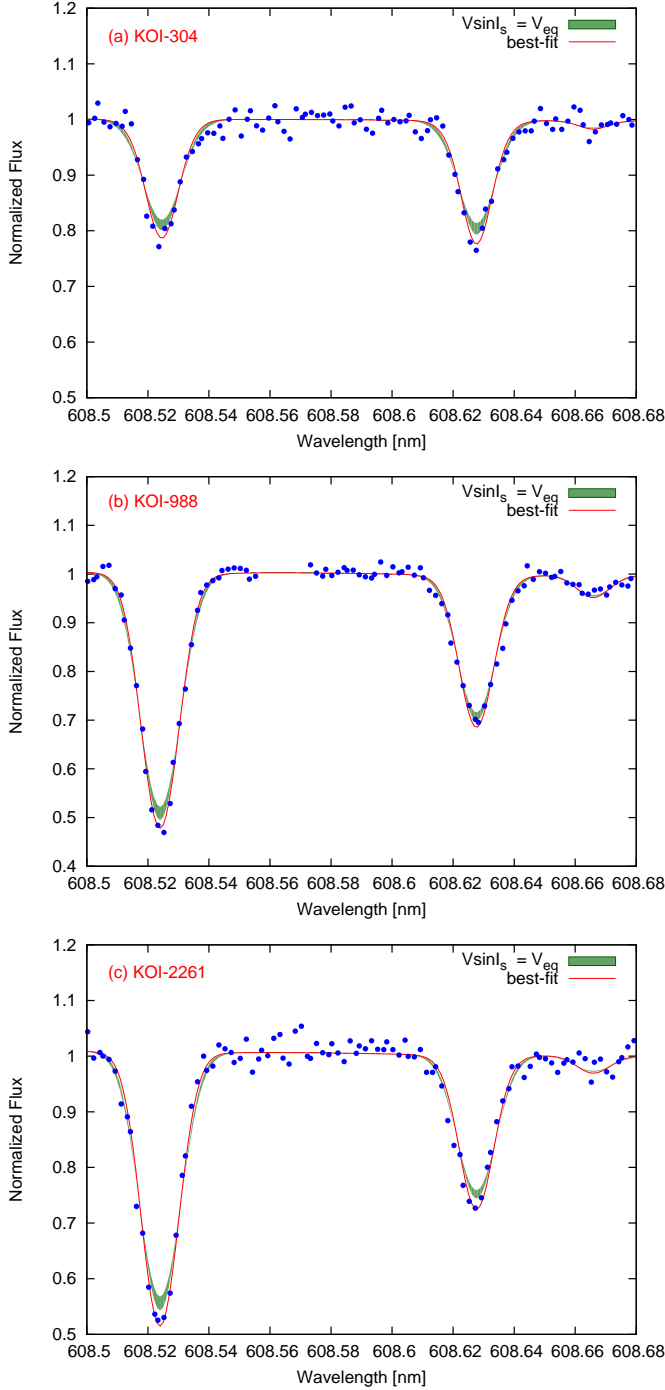


FIG. 8.— Part of the spectrum used for fitting $V \sin I_s$ for (a) KOI-304, (b) KOI-988, and (c) KOI-2261. In each panel, the blue dots show the observed spectrum and the red solid line indicates the best-fitting model computed by Equation (1). The green area indicates the range of model spectra satisfying $\sin I_s = 1$ (i.e., spin-orbit alignment) with a macroturbulent velocity ζ_{RT} differing by $\pm 15\%$ from the assumed value.

systems with misaligned stars. Each individual detection is statistically marginal, with less than 2σ confidence, but if the uncertainties have been accurately determined, then together it is likely that at least one system is misaligned. To quantify this statement we can compute the probability that all three multiple systems (KOI-304, 988, 2261) are well-aligned, defining this for convenience

to mean $I_s \geq 75^\circ$ ($\sin I_s \geq 0.9659$). Assuming that both V_{eq} and $V \sin I_s$ have uncertainties drawn from independent Gaussian distributions, with dispersions set equal to our quoted uncertainties, we calculate the probability for each system to have $0.9659 \leq \sin I_s$. If the lower and upper observation errors are different, we adopt a two-sided Gaussian with different upper and lower dispersions. We then compute the products of the resulting probabilities to find the net probability $p_{\text{all aligned}}$ that all three systems are aligned. We find $p_{\text{all aligned}} = 0.0025$, implying that at least one system among the three KOI's is very likely to have spin-orbit misalignment. This result cannot be definitive, though, given the possibility of systematic effects, or uncertainties that are correlated between different systems due to shared assumptions and techniques. Specifically, all the three systems fall on the regime where the measurement of $V \sin I_s$ tends to suffer from systematic effects ($V \sin I_s \lesssim 3 \text{ km s}^{-1}$). It is better to regard KOI-304, 988, and 2261 as candidate misalignments that are good targets for additional follow-up observations.

4.2. Distribution of Stellar Inclinations

In the previous subsection, we have seen that some of the systems (both single and multiple) may have spin-orbit misalignments. A natural question is “what is the fraction of misaligned systems?” Although the number of our samples is still small, a histogram of the observed I_s may be helpful to gain an insight into the underlying true distribution of the spin-orbit angle, just as the histogram of sky-plane angles was useful in the case of RM measurements (e.g., Pont et al. 2010). One issue concerning the conversion from the observed V_{eq} and $V \sin I_s$ to the distribution of I_s is that $\sin I_s \equiv V \sin I_s / V_{\text{eq}}$ could extend beyond unity due to measurement uncertainties. Theoretical distributions of $\sin I_s$ always satisfy $0 \leq \sin I_s \leq 1$, which inhibits a direct comparison between the theoretical and observed distributions. Here, we present a Bayesian method that avoids this problem by placing a prior on I_s .

Based on Bayes' theorem, the posterior probability distribution of V_{eq} and I_s is

$$P(V_{\text{eq}}, I_s | D) \propto P(D | V_{\text{eq}}, I_s) \cdot p_{\text{prior}}(V_{\text{eq}}) \cdot p_{\text{prior}}(I_s), \quad (8)$$

where “D” represents the observed data for V_{eq} and $V \sin I_s$ for each of the observed systems. We again assume that observational data for V_{eq} and $V \sin I_s$ follow the Gaussian distributions with their centers being $V_{\text{eq}} = p^{(i)}$ and $V \sin I_s = q^{(i)}$, and dispersions being $\sigma_p^{(i)}$ and $\sigma_q^{(i)}$, where i is the label of the system. In this case, the conditional probability $P(D | V_{\text{eq}}, I_s)$ is expressed as

$$P(D | V_{\text{eq}}, I_s) \propto \frac{1}{\sigma_p^{(i)}} \exp \left\{ -\frac{(p^{(i)} - V_{\text{eq}})^2}{2\sigma_p^{(i)2}} \right\} \frac{1}{\sigma_q^{(i)}} \exp \left\{ -\frac{(q^{(i)} - V_{\text{eq}} \sin I_s)^2}{2\sigma_q^{(i)2}} \right\}. \quad (9)$$

Assuming a uniform distribution for $p_{\text{prior}}(V_{\text{eq}})$ ($0 \leq V_{\text{eq}}$), we marginalize V_{eq} , so that we obtain the poste-

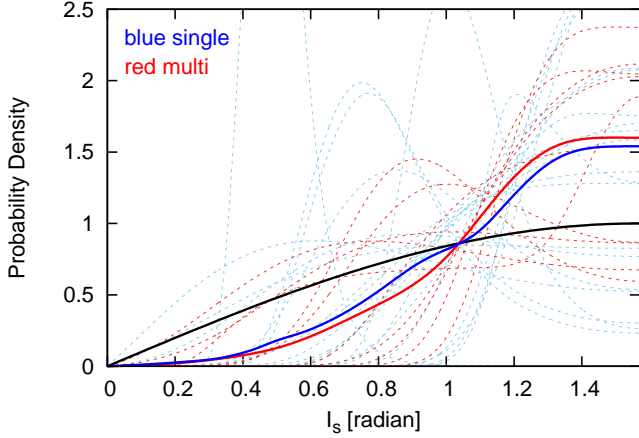


FIG. 9.— Posterior distributions of I_s computed by Equation (10). The dashed lines correspond to the result for each system in the sample (light-blue for single and light-red for multiple systems). The solid lines are averaged shapes of the posteriors for each category. The black solid curve represents the isotropic distribution of I_s for reference.

rior distribution for I_s :

$$P_i(I_s|D) \propto \int_0^\infty \frac{1}{\sigma_p^{(i)}} \exp\left\{-\frac{(p^{(i)} - V_{\text{eq}})^2}{2\sigma_p^{(i)2}}\right\} \frac{1}{\sigma_q^{(i)}} \exp\left\{-\frac{(q^{(i)} - V_{\text{eq}} \sin I_s)^2}{2\sigma_q^{(i)2}}\right\} dV_{\text{eq}} \cdot p_{\text{prior}}(I_s). \quad (10)$$

In case that the observed result for V_{eq} or $V \sin I_s$ has different upper and lower errors, we adopt two-sided Gaussian functions as in §4.1. When a prior defined in $0 \leq I_s \leq \pi/2$ (i.e., $0 \leq \sin I_s \leq 1$) is applied, the posterior $P_i(I_s|D)$ also could have a non-zero value in $0 \leq I_s \leq \pi/2$.

For each of the observed KOI systems, we compute the posterior distribution by Equation (10). We here assume the isotropic distribution for the prior on I_s (i.e., $p_{\text{prior}}(I_s) = \sin I_s$). This is physically unlikely considering the fact that many systems show a good spin-orbit alignment from measurements of the RM effect. However, the prior distribution is not so important since we do not attempt to quantitatively compare any distributions here (see the next subsection for a quantitative comparison). Instead, in order to visualize the distribution of I_s , we take the average of the posterior distributions by stacking $P_i(I_s|D)$ for observed systems. In Figure 9, we plot the averaged posterior distribution for either of single (blue) and multiple (red) KOI systems by the solid lines. These plots correspond to a sort of histogram of I_s considering that the peak of the posterior for each system likely represents the most plausible value of I_s , and all the systems have an equal weight. The two distributions (single and multiple) are similar, but single systems show a slightly wider distribution than that of multiple systems with small bumps at $I_s \lesssim 1.0$ radian ($\simeq 57^\circ$). For reference, we show by the black solid line the isotropic distribution of I_s . Note that in this analysis (and other statistical analyses below), we added the seven KOI systems reported in our previous campaign (KOI-257, 261, 262, 269, 280, 367, 974, Hirano et al. 2012a) to the list of targets subjected to the statistical

analysis.

It should be stressed that our observed systems (both single and multiple) have no hot Jupiters and all the planet candidates are Earth-sized or Neptune-sized ones. Little is known about the spin-orbit angle for these classes of planets, and the observed distribution of the angle could be more or less different from that for close-in giant planets. We also note that while hot Jupiters are in general isolated single planets (Steffen et al. 2012), many of single transiting systems in our sample may actually be multiple systems (e.g., transits of outer planets are unobservable due to geometry). This possibility makes it difficult to interpret the comparison of I_s for single and multiple systems.

4.3. Statistical Tests

Figures 5 and 9 suggest that the observed distributions of I_s differ from an isotropic distribution and also differ from perfect spin-orbit alignment. However, the degree to which the observed distributions are different from or similar to each other is quantitatively not clear. Also, we are interested in whether single-transiting and multiple-transiting systems have the same distribution for I_s . We test the following two hypotheses with the Kolmogorov-Smirnov (KS) test:

- (a) the observed values of I_s (all systems) are drawn from an isotropic distribution,
- (b) the observed distributions of I_s for single and multiple systems are the same.

We perform a Monte-Carlo simulation to implement the KS tests. We take the following steps based on the observed values of V_{eq} and $V \sin I_s$.

1. First, we randomly generate $(V_{\text{eq}}^{(i)}, V \sin I_s^{(i)})$ for system i assuming Gaussian distributions (two-sided Gaussians if needed) with dispersions set equal to the quoted measurement uncertainties.
2. We then compute $I_s^{(i)} \equiv \arcsin(V \sin I_s^{(i)} / V_{\text{eq}}^{(i)})$ for each system. Whenever $V \sin I_s^{(i)} > V_{\text{eq}}^{(i)}$, we set $I_s = 90^\circ$.
3. Based on the set of $\{I_s^{(i)}\}$ with all the systems in the sample, we implement the KS test and record the value of D (the largest difference between the two cumulative distributions).
4. We repeat the preceding steps (1 to 3) 10^6 times, recording the values of D and finding the median and standard deviation of the collection of D values, and the corresponding probability that the two distributions may be the same, which we denote by $p(D > D_{\text{obs}})$.

We first test the hypothesis (a). The two distributions tested are the observed distribution of $\{I_s^{(i)}\}$ and the theoretical isotropic distribution. As a result of implementing the steps 1 - 4, we obtain $D_{\text{obs}} = 0.344_{-0.063}^{+0.094}$, corresponding to $p(D > D_{\text{obs}}) = 0.00071_{-0.00071}^{+0.00912}$. Therefore, the hypothesis (a) is highly unlikely, and this result should indicate that the stellar equators in our sample

are preferentially edge-on, suggesting a tendency toward spin-orbit alignment.

In the second test, the two tested distributions are both observed distributions of I_s , one for single and the other for multiple systems. Implementing the KS test, we find $D_{\text{obs}} = 0.255^{+0.091}_{-0.065}$, which corresponds to $p(D > D_{\text{obs}}) = 0.665^{+0.265}_{-0.380}$. This result indicates that the two observed distributions are not significantly different, and might be drawn from the same distribution. To see this result is robust, we repeat the steps 1-4, implementing instead of the KS test the K -sample Anderson-Darling (AD) test (e.g., Hou et al. 2009), which has more sensitivity around the tails of distributions. As a consequence, the p -value of $0.519^{+0.123}_{-0.277}$ is obtained, which also implies the two observed distributions are not significantly different. The results of these statistical tests cannot corroborate recent findings by RM measurements, asteroseismology, and the spot-crossing method that multiple-transiting systems preferentially show a good spin-orbit alignment (Sanchis-Ojeda et al. 2012; Hirano et al. 2012b; Albrecht et al. 2013; Chaplin et al. 2013). However, it is premature to conclude that our result actually contradicts the previous findings; more systems are needed (particularly multiple-transiting systems) for a more definitive conclusion. The exact sample size that will be required depends on the true distribution of the spin-orbit angle.

5. SUMMARY

In this paper, we investigated the stellar inclinations for KOI systems by combining the rotation periods estimated from the *Kepler* photometry and projected rotational velocities $V \sin I_s$ determined from Subaru spectroscopy. We constrained the stellar inclination I_s for 25 KOI systems, and discussed statistical properties using all the systems observed so far by Subaru. There are several implications that we list here.

1. Based on the KS test, the observed distribution of I_s is significantly different from an isotropic distribution, suggesting that the direction of stellar spin is correlated with the planetary orbital axis. Spin-orbit alignment has been reported for many transiting systems, but most of the systems with RM measurements have hot (warm) Jupiters. Our measurements pertain to Neptune-sized or Earth-sized planets, which are likely to have a different history of formation and migration than giant planets. In particular the smaller planets are not as likely to have strong tidal interactions with their host stars, and therefore the orbital orientations may reflect more primordial conditions.
2. A certain fraction of the systems show possible spin-orbit misalignments ($I_s \lesssim 75^\circ$). We had a closer look at the seemingly misaligned multiple transiting systems (KOI-304, 988, and 2261), and they all survived as candidates for misaligned stars.
3. The statistical tests indicate that the observed distributions of I_s for single and multiple transiting systems are not significantly different. The sensitivity of this test is limited, however, by the small

number of multiple systems (only 11). The averaged posterior distribution shown in Figure 9 suggests that the single transiting systems might have a larger fraction of spin-orbit misalignment. This should be confirmed or refuted by further observations of transiting systems.

As Hirano et al. (2012a) noted, our present method cannot discriminate the state of $I_s = -90^\circ$ (retrograde orbit) from that of $I_s = +90^\circ$ (prograde orbit). The degeneracy between $I_s = -90^\circ$ and $I_s = +90^\circ$ would certainly make the fraction of misaligned systems look smaller than the real fraction (systems with $I_s \approx -90^\circ$ would appear to be aligned in Figure 5), but it does not affect the statements 1. and 2. of the above summary. In addition, given the fact that the measurements of the RM effect so far have not revealed a strong evidence of a “perfectly anti-aligned” system (i.e., $\lambda \approx \pm 180^\circ$), it is expected to be a rare case to find a system with $I_s \approx -90^\circ$. All the other retrograde cases (e.g., $-75^\circ \lesssim I_s \lesssim 0^\circ$) are actually regarded as “misaligned” in Figure 5 as in the case of prograde orbits. In other words, our methodology gives the lower limit on the fraction of misaligned systems.

One task left is the confirmation of the planetary nature for the KOI planet candidates on which we focused in this paper. While the false positive rate for KOI multiple systems is proved to be negligible (Lissauer et al. 2012), any contamination from background/foreground source(s) leads to a wrong determination of the rotation period and/or spectroscopic parameters. A deep direct imaging search for companions around the KOI stars would be helpful both in terms of putting a constraint on the magnitude of contamination and identifying the possible cause of spin-orbit misalignment.

This paper is based on data collected at Subaru Telescope, which is operated by the National Astronomical Observatory of Japan. We acknowledge the support for our Subaru HDS observations by Akito Tajitsu, a support scientist for the Subaru HDS. T.H. expresses special thanks to Masayuki Kuzuhara, Yuka Fujii, Akihiko Fukui, and Yasushi Suto for fruitful discussions on this subject. The data analysis was in part carried out on common use data analysis computer system at the Astronomy Data Center, ADC, of the National Astronomical Observatory of Japan. T.H. and Y.H.T. are supported by Japan Society for Promotion of Science (JSPS) Fellowship for Research (PD:25-3183, DC1: 23-3491). J.N.W. and R.S.O. gratefully acknowledge support from the NASA Origins program (NNX11AG85G) and Kepler Participating Scientist program (NNX12AC76G). N.N. acknowledges support by the NAOJ Fellowship, the NINS Program for Cross-Disciplinary Study, and Grant-in-Aid for Scientific Research (A) (No. 25247026) from the Ministry of Education, Culture, Sports, Science and Technology (MEXT) of Japan. We acknowledge the very significant cultural role and reverence that the summit of Mauna Kea has always had within the indigenous people in Hawai'i.

REFERENCES

- Akeson, R. L., et al. 2013, *PASP*, 125, 989
- Albrecht, S., Winn, J. N., Marcy, G. W., Howard, A. W., Isaacson, H., & Johnson, J. A. 2013, *ApJ*, 771, 11
- Albrecht, S., et al. 2012, *ApJ*, 757, 18
- Batalha, N. M., et al. 2013, *ApJS*, 204, 24
- Borucki, W. J., et al. 2010, *Science*, 327, 977
- Brown, T. M., Latham, D. W., Everett, M. E., & Esquerdo, G. A. 2011, *AJ*, 142, 112
- Bruntt, H., et al. 2010, *MNRAS*, 405, 1907
- Chaplin, W. J., et al. 2013, *ApJ*, 766, 101
- Collier Cameron, A. 2007, *Astronomische Nachrichten*, 328, 1030
- Désert, J.-M., et al. 2011, *ApJS*, 197, 14
- Doyle, L. R., Wilcox, T. J., & Lorre, J. J. 1984, *ApJ*, 287, 307
- Fabrycky, D., & Tremaine, S. 2007, *ApJ*, 669, 1298
- Gray, D. F. 2005, *The Observation and Analysis of Stellar Photospheres*, ed. Gray, D. F.
- Hébrard, G., et al. 2008, *A&A*, 488, 763
- Hirano, T., Narita, N., Sato, B., Winn, J. N., Aoki, W., Tamura, M., Taruya, A., & Suto, Y. 2011a, *PASJ*, 63, L57
- Hirano, T., Sanchis-Ojeda, R., Takeda, Y., Narita, N., Winn, J. N., Taruya, A., & Suto, Y. 2012a, *ApJ*, 756, 66
- Hirano, T., Suto, Y., Winn, J. N., Taruya, A., Narita, N., Albrecht, S., & Sato, B. 2011b, *ApJ*, 742, 69
- Hirano, T., et al. 2012b, *ApJ*, 759, L36
- Hou, A., Parker, L. C., Harris, W. E., & Wilman, D. J. 2009, *ApJ*, 702, 1199
- Huber, D., et al. 2013, *ArXiv e-prints*
- Kurucz, R. 1993, *ATLAS9 Stellar Atmosphere Programs and 2 km/s grid*. Kurucz CD-ROM No. 13. Cambridge, Mass.: Smithsonian Astrophysical Observatory, 1993., 13
- Lai, D., Foucart, F., & Lin, D. N. C. 2011, *MNRAS*, 412, 2790
- Lin, D. N. C., Bodenheimer, P., & Richardson, D. C. 1996, *Nature*, 380, 606
- Lissauer, J. J., et al. 2012, *ApJ*, 750, 112
- McQuillan, A., Aigrain, S., & Mazeh, T. 2013a, *MNRAS*, 432, 1203
- McQuillan, A., Mazeh, T., & Aigrain, S. 2013b, *ApJ*, 775, L11
- Nagasawa, M., & Ida, S. 2011, *ApJ*, 742, 72
- Naoz, S., Farr, W. M., Lithwick, Y., Rasio, F. A., & Teyssandier, J. 2011, *Nature*, 473, 187
- Narita, N., Sato, B., Hirano, T., & Tamura, M. 2009, *PASJ*, 61, L35
- Narita, N., et al. 2007, *PASJ*, 59, 763
- Nutzman, P. A., Fabrycky, D. C., & Fortney, J. J. 2011, *ApJ*, 740, L10
- Ohta, Y., Taruya, A., & Suto, Y. 2005, *ApJ*, 622, 1118
- Pont, F., et al. 2010, *MNRAS*, 402, L1
- Press, W. H., & Rybicki, G. B. 1989, *ApJ*, 338, 277
- Queloz, D., Eggenberger, A., Mayor, M., Perrier, C., Beuzit, J. L., Naef, D., Sivan, J. P., & Udry, S. 2000, *A&A*, 359, L13
- Sanchis-Ojeda, R., Winn, J. N., Holman, M. J., Carter, J. A., Osip, D. J., & Fuentes, C. I. 2011, *ApJ*, 733, 127
- Sanchis-Ojeda, R., et al. 2012, *Nature*, 487, 449
- . 2013, *ApJ*, 775, 54
- Schlaufman, K. C. 2010, *ApJ*, 719, 602
- Smith, J. C., et al. 2012, *PASP*, 124, 1000
- Steffen, J. H., et al. 2012, *Proceedings of the National Academy of Science*, 109, 7982
- Stumpe, M. C., et al. 2012, *PASP*, 124, 985
- Tajitsu, A., Aoki, W., & Yamamuro, T. 2012, *PASJ*, 64, 77
- Takeda, Y., Ohkubo, M., & Sadakane, K. 2002, *PASJ*, 54, 451
- Takeda, Y., Ohkubo, M., Sato, B., Kambe, E., & Sadakane, K. 2005, *PASJ*, 57, 27
- Triaud, A. H. M. J., et al. 2010, *A&A*, 524, A25+
- Valenti, J. A., & Fischer, D. A. 2005, *ApJS*, 159, 141
- Walkowicz, L. M., & Basri, G. S. 2013, *MNRAS*
- Winn, J. N., Fabrycky, D., Albrecht, S., & Johnson, J. A. 2010, *ApJ*, 718, L145
- Winn, J. N., Johnson, J. A., Albrecht, S., Howard, A. W., Marcy, G. W., Crossfield, I. J., & Holman, M. J. 2009, *ApJ*, 703, L99
- Winn, J. N., et al. 2005, *ApJ*, 631, 1215
- Wolf, A. S., Laughlin, G., Henry, G. W., Fischer, D. A., Marcy, G., Butler, P., & Vogt, S. 2007, *ApJ*, 667, 549
- Wu, Y., & Murray, N. 2003, *ApJ*, 589, 605
- Yi, S., Demarque, P., Kim, Y.-C., Lee, Y.-W., Ree, C. H., Lejeune, T., & Barnes, S. 2001, *ApJS*, 136, 417